FISEVIER

Contents lists available at ScienceDirect

Materials Today Chemistry

journal homepage: www.journals.elsevier.com/materials-today-chemistry/



Ni-based overall water splitting electrocatalysts prepared via laserablation-in-liquids combined with electrophoretic deposition



A. Shukla a, S.C. Singh a, b, *, C.S. Saraj a, c, G. Verma a, C. Guo b, **

- ^a The Guo China-US Joint Photonics Laboratory (GPL), Changchun Institute of Optics, Fine Mechanics and Physics (CIOMP), Chinese Academy of Sciences (CAS), Changchun 130033, PR China
- ^b The Institute of Optics, University of Rochester, Rochester, NY 14627, USA
- ^c University of Chinese Academy of Sciences, Beijing 100049, China

ARTICLE INFO

Article history: Received 18 August 2021 Received in revised form 9 November 2021 Accepted 13 November 2021 Available online 28 December 2021

Keywords:
Laser ablation in liquids
Electrophoretic deposition
Electric-field-assisted deposition
Overall water splitting
Nickel oxide/nickel hydroxide
nanocomposite

ABSTRACT

Synthesis of fine nanoparticles (NPs) with surface-active sites free from undesired chemical residues is the key to drive chemical kinetics. However, active sites of chemically produced NPs are limited because of the adsorption of chemical residues. Therefore, the development of a physical approach to produce NPs having surfaces free from chemical contamination is imperative to electrochemical water splitting. Here, we present a physical top-down approach where suspended NPs generated via pulsed laser ablation in liquids are electrophoretic deposited on a substrate to fabricate ready-to-use electrocatalysts for overall water splitting. Three different laser pulse energies were used to ablate Ni plate in pure water or aqueous media of 1M polyethylene glycol (PEG) to produce six different colloidal solutions of NPs. The samples produced in the water at higher laser pulse energies have Ni/NiO phase in abundance, while those produced in PEG dominate Ni/Ni(OH)2 phase. Among all the electrophoretically fabricated electrocatalysts, Ni-Di-70 is the best performer in overall water splitting, while Ni-P-30 is the worse. We believe that the selective adsorption of H*, responsible for hydrogen evolution reaction, at Ni sites, and OH- ions, oxygen evolution intermediate, at NiO sites of Ni/NiO interface increase hydrogen and oxygen generation performances of Ni-Di-70 sample. The poor performance of PEG produced electrocatalysts is attributed to the combined effects of the formation of a larger assembly of NPs and adsorption of PEG molecules on the active sites.

© 2021 Published by Elsevier Ltd.

1. Introduction

Electrochemical water splitting is an efficient way to convert and store intermittent electrical energy into hydrogen and oxygen, storable fuels, through hydrogen evolution reaction (HER) and oxygen evolution reaction (OER), respectively, but require suitable electrocatalysts [1–4]. Platinum and precious metal oxides, such as RuO₂ and IrO₂, are considered as the best-performing HER and OER catalysts, respectively, owing to their low overpotential to drive these reactions and their high chemical and corrosion resistance in the electrolyte solution [5–8]. However, scarcity and high cost limit

E-mail addresses: ssingh49@ur.rochester.edu (S.C. Singh), guo@optics.rochester.edu (C. Guo).

their applications in electrochemical water splitting for scalable hydrogen and oxygen productions [9,10]. Thus, the search for earthabundant and non-precious catalysts for high-efficiency overall water splitting with long-term stability in an electrolyte solution has attracted significant research attention in recent years [11–29]. A range of non-noble and non-precious metal-based electrocatalysts are researched for this purpose recently, including transition metal dichalcogenides [11–14], transition metal oxides/hydroxides [15–22], layered double and triple hydroxides [23–28], carbides and nitrides [29], and sulfides and phosphides [30–32].

Recently, nickel-based compounds, such as NiX (where X: O, S, Se, (OH)₂ and OOH), have attracted intensive attention as an earthabundant electrocatalyst because of their strong capability to adsorb protons and hydrides on the nickel active sites to make favorable conditions for the X sites of the structure to bind with reaction intermediates of water splitting [23,33–40]. For example, Ni(OH)₂ \rightarrow NiOOH and NiOOH \rightarrow Ni(OH)₂ chemical reactions are used for hydrogen and oxygen generations, respectively [35]. Similarly, NiOOH

^{*} Corresponding author. The Guo China-US Joint Photonics Laboratory (GPL), Changchun Institute of Optics, Fine Mechanics and Physics (CIOMP), Chinese Academy of Sciences (CAS), Changchun 130033, PR China.

^{**} Corresponding author.

on Ni was used as an efficient overall water splitting electrocatalyst in alkaline media [37]. In general, catalyst materials are produced using a multistep bottom-up approach that involves hazardous chemicals and toxic bi-products having negative impacts on water sources and on the environment [41,42]. To reduce the impact of hazardous chemical waste on the environment, several green approaches are researched recently, where a chemical precursor is reduced using biological extracts [43,86]. Despite multiple rounds of cleaning and centrifugation, chemical residues adsorbed on active sites of electrocatalysts limits their electrochemical surface area (ESCA) and hence water splitting performance.

Pulsed laser ablation (PLA) of solid target or suspended particles in liquids is a one-step, one-pot, and environmental-friendly topdown approach to produce nanoparticles (NPs) with active sites free from chemical adsorbents [44–48]. The NPs produced by this approach have a surface charge that provides colloidal stability in the solution through Coulombic repulsion [46,49,50]. Due to their purity and colloidal stability, PLA in liquid produced NPs have recently used as nanofertilizers [88-90], biological and medical applications [44]. Electrocatalytic applications of these NPs generally require their separation from the solution through centrifugation, dispersion in alcohol and Nafion mixture, and redeposition on a glassy carbon electrode for electrochemical measurements [51,52] and battery applications [87]. These multistep and complex processes and use of Nafion can be avoided through electrophoretic deposition (EPD) of surface charged NPs directly on a conductive substrate to make ready-to-use working electrodes for overall water splitting [53,54], battries, and supercapacitors [87]. However, very little research is carried out to date to electrophoretically deposit NPs on a substrate to make electrodes [55]. The rate of deposition of NPs on the substrate for a given applied electric field $(\Delta V/d)$; where ΔV is applied potential difference between two electrodes and d is the distance between them) depends on the surface charge on NPs, their mass, their density in the solution, and viscosity and permittivity of the liquid medium.

Here, in this article, we present the EPD of PLA in liquids produced Ni/NiO/Ni(OH)₂ NPs on indium tin oxide (ITO) coated glass substrate to make ready-to-use electrocatalysts for overall water splitting. The colloidal solutions of Ni/NiO/Ni(OH)₂ NPs were first prepared using pulsed nanosecond laser ablation of Ni target in double-distilled water or water/polyethylene glycol (PEG) mixture followed by their EPD on ITO coated glass substrate. The pulse energy of the laser beam is varied between 30 and 70 mJ/pulse to control elemental composition, size, morphology, and hence electrochemical properties of Ni/NiO/Ni(OH)₂ nanocomposite. The electrocatalytic material produced in double distilled water at 70 mJ/pulse energy, termed as Ni-Di-70 hereafter, showed the best HER and OER performances, while that produced at 30 mJ/pulse energy in aqueous medium of PEG, termed as Ni-P-30 hereafter, is the worse. We believe that selective adsorption of H* and OH* at Ni and NiO sites, respectively, of Ni/NiO interface synergistically increase hydrogen and oxygen generation performances of Ni-Di-70 samples. The poor performance of all PEG-produced electrocatalysts is attributed to the combined effects of the formation of a larger assembly of NPs and adsorption of PEG molecules on the active sites.

2. Experimental section

2.1. Synthesis of $Ni/NiO/Ni(OH)_2$ nanocomposite electrochemical materials

2.1.1. Materials

Pure nickel disc 99.999% (Advanced materials professional manufacture, China), PEG (Alladin, China), and deionized water (DI) were used without further purification.

2.1.2. Synthesis of colloidal solutions of NPs and their diEPD

Similar to our previous works, Ni/NiO/Ni(OH)₂ electrocatalytic materials were synthesized using PLA of nickel target submerged in double distilled water or water and PEG mixture [56-59]. In brief, a pure nickel disc placed at the bottom of a glass vessel containing 20 ml of liquid (deionized (DI) water or 1 M aqueous solution of PEG) was allowed to irradiate with the focused output of 1064 nm wavelength of the laser beam from a pulsed Nd: YAG laser (O-smart 850 Nd: YAG) operating at 10 ns pulse width, 10 Hz repletion rate for 1 h (Fig. 1). For a given liquid medium, 30, 50, or 70 mJ/pulse energy was used to prepare three colloidal solutions of NPs samples in distilled water and three in water/PEG mixture. The samples produced in DI water are named Ni-Di-30, Ni-Di-50, Ni-Di-70, while those produced in aqueous media of PEG are named Ni-P-30, Ni-P-50, and Ni-P-70. Thus, obtained colloidal solutions of NPs were immediately transferred in the ultrasonication bath for dispersion and EPD on ITO coated glass substrate. The applied electric field is fixed to 25 V/cm using a dc regulated power supply. The solution of NPs was continuously ultrasonicated during the EPD.

2.2. Characterizations of as-synthesized colloidal solution

UV—Vis absorption spectra of as-synthesized colloidal solutions of NPs were recorded using Agilent Cary 3000 double beam spectrophotometer. Hemispherical transmittance of NPs deposited on ITO coated glass substrate was also measured using Agilent Cary 3000 double beam spectrophotometer combined with a 50 mm diameter integrating sphere. The nanomaterials samples electrophoretically deposited on ITO-coated glass substrate was characterized for crystallographic and phase using Bruker D8 Focus X-ray diffractometer with CuK α line ($\lambda=1.5406$ Å) X-ray line source. Hitachi S4800 scanning electron microscope (SEM) was used for surface morphological investigation, while RM2000 Horiba Confocal Raman Spectrometer with 785 nm excitation laser was used for Raman spectroscopic measurements.

2.3. Overall water splitting and electrochemical impedance spectroscopic (EIS) measurements

Electrochemical measurements were performed in a threeelectrode system using an electrochemical workstation (Biological, Model VMP3). A saturated calomel electrode (SCE) was used as a reference electrode; a platinum wire was used as a counter electrode, and electrophoretically deposited catalysts on a $0.5~\text{cm} \times 0.5~\text{cm}$ area of ITO coated glass substrate was used as a working electrode. Around 3 mg of electrocatalyst was electrophoretically on the working electrode. A fresh aqueous alkaline solution of KOH (1 M) with a pH value of 13.5 was used as an electrolyte in all the measurements. Electrocatalysts were prestabilized using 30-60 cycles of cyclic voltammetry (CV) in the potential range from -0.8 to +0.2 V (vs. SCE) at a scan rate of 20 mV/s. After the pre-stabilization step, linear sweep voltammetry (LSV) was measured with a sweep rate of 20 mVs⁻¹ in the potential range from -0.8 to + 0.2 V (vs. SCE). Expression $E_{RHE} =$ $E_{SCE} + E_{SCF}^{0} + 0.0592*pH$, where $E_{SCF}^{0} = 0.242 V$, was used to translate V vs. SCE to V vs. reverse hydrogen electrode (RHE). For OER, electrochemical impedance spectroscopy (EIS) was measured under an ac signal of 10 mV amplitude in the frequency range of 0.01-100,000 Hz superimposed on a dc potential of 1.2402 V (vs. RHE). Similarly, for the HER, EIS measurements were carried out using an ac signal of 10 mV in a frequency range of 0.01-100,000 Hz superimposed on a dc signal of -0.5 V (vs. RHE).

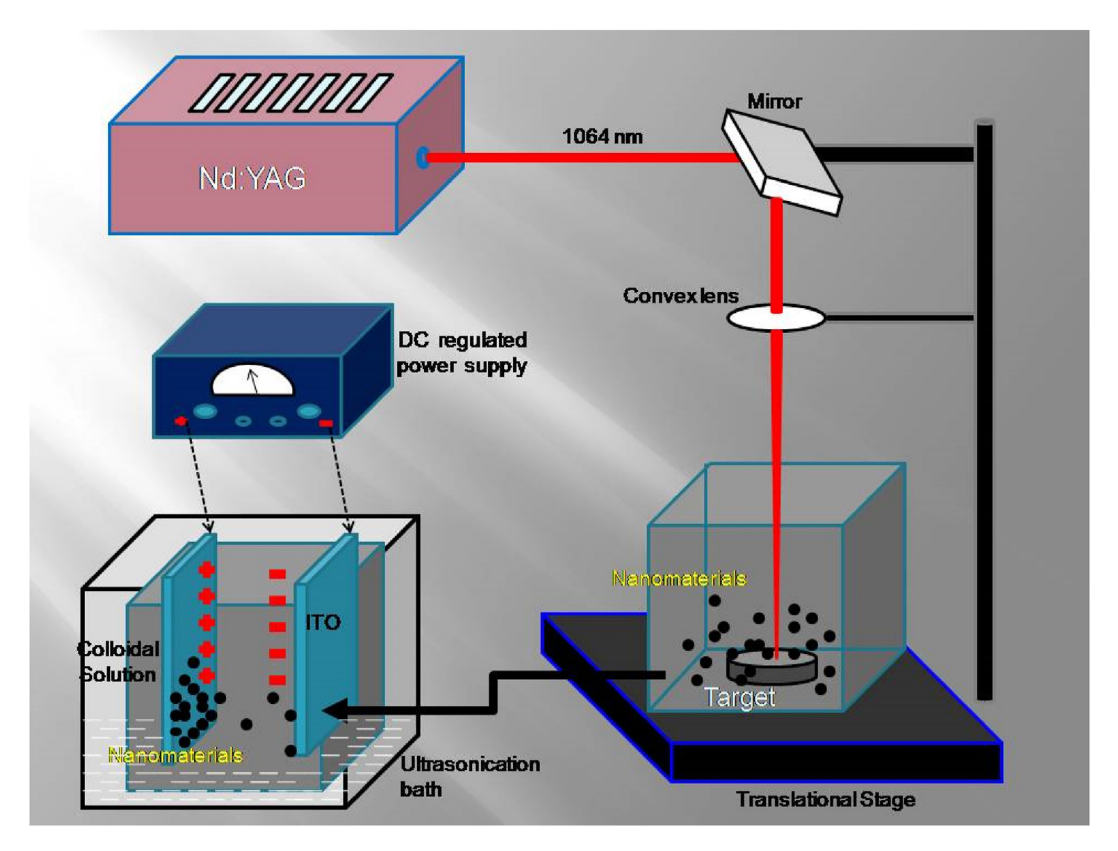


Fig. 1. Schematic for the experimental setup used for the synthesis of Ni/NiO/Ni(OH)₂ NPs using pulsed laser ablation method followed by electrophoretic deposition. NP, nanoparticle.

3. Results and discussions

3.1. UV-visible absorption spectra of as-produced colloidal solution of NPs

UV-visible absorption spectroscopy of as-obtained colloidal solution of NPs can be used to determine the relative concentration, average size, and distribution of NPs suspended in the solution. Generally, NPs production increases with an increase in laser pulse energy until laser fluence reaches the ablation threshold of water, where laser energy non-linearly gets absorbed by water plasma before reaching the target surface [47]. The UV-visible absorption spectra of as-synthesized colloidal solution of NPs produced in 1 M aqueous solution of PEG and double distilled water are shown in Fig. 2. The photographs of the corresponding colloidal solutions of NPs are also shown in the insets. A strong absorption peak at ~200 nm with a shoulder at ~290 nm shows synthesis of <10 nm Ni NPs with <1 nm thick layer of oxide/hydroxide shell in all the NPs solutions [60]. For the PLA of Ni in the aqueous media of PEG, an increase in the absorbance at 200 nm with an increase in the laser pulse energy from 30 mJ/pulse to 50 mJ/pulse shows a higher yield of NPs synthesis with a slight increase in the size of particles. Further increase in the laser pulse energy from 50 mJ/pulse to 70 mJ/pulse causes a decrease in the absorbance at 200 nm, possibly because of coagulation of the larger-sized NPs followed by their sedimentation that reduces the density of particles in the suspension. The sedimentation of NPs can be seen at the bottom of the sample (Ni-P-70) produced at 70 mJ/pulse energy (inset Fig. 2(a)). Similarly, in the case of PLA of Ni target in double-distilled water (Fig. 2(b)), deep UV absorbance at ~200 nm increases by ~ 1.5 times with an increase in the laser pulse energy from 30 to 50 mJ/pulse (1.67 times). However, further, increase in the laser pulse energy to 70 mJ/pulse drastically reduced the absorbance at 200 nm that may be due to the combined effect of sedimentation of the larger size of NPs and non-linear absorption of laser pulse energy through the breakdown of water in front of the target surface, i.e. through liquid-plasma-induced target shielding [47]. No obvious sedimentation of NPs at the bottom of the vessel (inset Fig. 2(b)) demonstrates dominance of the liquid-plasma-induced target shielding over the coagulation and sedimentation of the particles.

Laser ablation of a solid target at the solid-liquid interface produces plasma of the solid target containing fast-expanding electrons and comparatively slower propagating ions and neutrals from the target surface. A large density of electrons gets ejected even before the plasma formation through photoelectric effects. These excess electrons are present in the liquid. In PLA in liquids, the NPs nucleate and grow at the plasma-liquid interface and inside the plasma where density of the plasma is high and temperature is low. the most favorable condition for nucleation and growth. The asproduced NPs get injected into the bulk liquid, where excess electrons get deposited on its surface to produce negatively surface charged NPs that increase the colloidal stability of the solution [47]. The plasma-induced plasma that forms through thermal dissociation of the surrounding water in front of the laser-produced plasma has H⁺ and OH⁻ species, where H⁺ species expands faster because of their lower mass, while OH may get adsorbed on the NPs surface to give them negative surface charge. The surface charge of NPs produced through laser ablation in liquids, does not matter produced at the plasma-liquid interface or in the bulk plasma, can be retained for several months that maintain colloidal stability of the solution.

The rate of EPD of NPs on a conductive substrate can be estimated by measuring the current density passing through the corresponding colloidal solution of NPs. At a given applied electric field

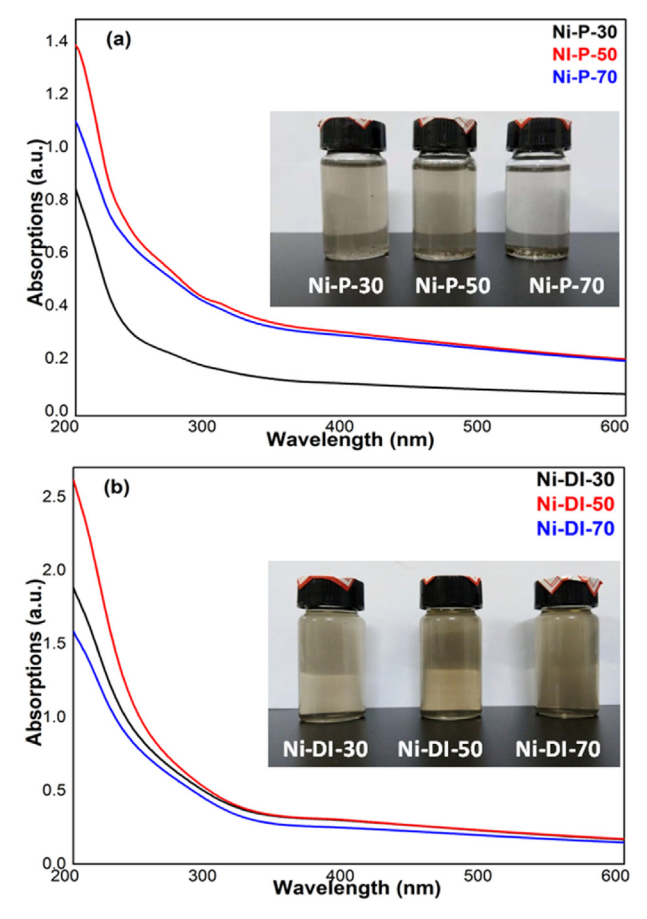


Fig. 2. UV—visible absorption spectra and photographs of colloidal solution of Ni/NiO/Ni(OH)₂ NPs produced in (**a**) 1M solution of PEG in deionized water and in (**b**) deionized water at 30 mJ, 50 mJ, and 70 mJ/pulse energy. NP, nanoparticle; PEG, polyethylene glycol.

and liquid medium parameters, the current passing through the solution and hence the rate of deposition depend on the density of NPs, surface charge, and mass of the particle following the expression: $i = neAv_d$; where n is the density of NPs, e is the surface charge on the NPs, A is the area of electrodes, and $v_d = \mu E$ is the drift velocity. Here, μ is the mobility of NPs and E is the electric field (E = V/d; where V is applied potential and d is the separation between electrodes). The density (n) of NPs produced in water and aqueous media of PEG was estimated through the difference in the mass of the same volume of liquid before (without NPs) and after laser ablation (with NPs) (Fig. 3(a)). A schematic of the experimental setup, used to measure the current density of the solution of NPs, is shown in Fig. 3(b (i)). An equivalent circuit for EPD is shown in Fig. 3(b (ii)). Following Kirchhoff's law; $R_s + R_d = V/i$; where Rs and Rd are resistances of solution and the deposited film respectively and V and i are applied voltage and current in the circuit, respectively. The current density $j\left[\left(\frac{i}{A}\right) = ne\mu E\right]$ vs. E curves corresponding to different solutions of NPs produced in water and aqueous media of PEG are shown in Fig. 3(c) and (d) respectively. The linear fit of J - E curves can be used to get electrical conductivity (dj/dE = ne μ = σ) of the corresponding solution of NPs. At a given electric field, the solution of NPs with higher electrical conductivity should have a higher rate of deposition. It is worth mentioning that the colloidal solution of NPs, in both ablation media, produced at lower laser pulse energies have comparatively higher electrical conductivity ($ne\mu$) (Fig. 3(e) and (f)), even these solutions have a lower density (n) of NPs (Fig. 3(a)). These measurements show that the NPs produced at lower pulse energies have higher values of $e\mu$ possibly because of the smaller size of NPs in the solution. The value of E-field corresponding to peak current density (j_{max}) can be used to compare the average size of NPs in the solution. For example, the observation of j_{max} at higher electric fields in the colloidal solutions of NPs produced at 70 mJ/pulse energies (Fig. 3(c) and (d)) shows the presence of some larger sizes of NPs that require comparatively higher electric force to transfer them from solution to the substrate.

The relative density of NPs electrophoretically deposited on a transparent substrate and hence the thickness of NPs film can be compared using hemispherical transmittance measurements (Fig. 4(a)). Direct and scattered light photons passing through the layers of NPs deposited on ITO coated glass substrate is collected through an integrating sphere and delivered to a photodetector. The transmittance spectra of NPs electrophoretically deposited on ITO coated glass substrate from the colloidal solutions of NPs prepared under different experimental conditions and a bare ITO coated glass substrate are shown in Fig. 4(b). All NPs samples were electrophoretically deposited under the same experimental conditions (25 V dc voltage, 1 cm distance between electrodes). The ITO coated glass substrate has nearly 100% transmittance in the studied spectral range; however, NPs film electrophoretically deposited from Ni-PEG-30 colloidal solution has ~20% transmittance at 800 nm that monotonically decreases with wavelength and attains a plateau of ~2% in the spectral range of 400-300 nm. The lower transmittance of Ni-PEG-30/ITO film shows the deposition of a larger density of NPs because of the higher electrical conductivity of the solution (Fig. 3). As discussed in the previous paragraph, a larger amount of NPs deposition in a given liquid medium is related to the density, surface charge, and mobility of the NPs in the solution. The colloidal solution of NPs produced at a higher laser pulse energy (50 mJ/pulse; Ni-PEG-50) has a comparatively higher density of NPs in the solution (Fig. 3(a)), but the higher transmission of electrophoretically deposited films shows comparatively smaller thickness. This is possibly related to the smaller electrical conductivity of the corresponding solution. Table 1 presents the area of NPs deposited on ITO-coated glass substrate from different colloidal solutions.

3.2. Structural and phase characterizations of electrophoretically deposited electrocatalytic materials

The X-ray diffraction (XRD) patterns of different electrocatalysts samples deposited on ITO coated glass along with corresponding standard diffraction lines are presented in Fig. 5. The vertical lines show standard diffraction lines of 3Ni(OH)2.2H2O (black), NiOOH(red), NiO(blue), and Ni (green) for reference. The XRD measurement illustrates the presence of mixed-phase of Ni. NiOOH. and Ni(OH)₂ in NPs produced in water and aqueous media of PEG. The diffraction peaks observed in the sample Ni-P-30 mainly comprised of a mixed compound with pure nickel, nickel-oxyhydroxide (NiOOH) JCPDF-270956, and nickel hydroxide hydrate {3Ni(OH)₂.2H₂O} JCPDF-220444 [61]. The intensity of diffraction peaks of NPs in the Ni-P-30 sample shows that 3Ni(OH)₂.2H₂O phase is in dominance over pure Ni and NiOOH phases. The XRD pattern of sample Ni-Di-70 has two dominant peaks at 2θ values of ~44° and 51° corresponding to Ni (1 1 1) and Ni (2 0 0) reflections, respectively, (COD: 1512526) along with diffraction peaks corresponding to (111) and (200) peaks of NiO and (002) and (110) peaks of 3Ni(OH)2.2H2O. The XRD spectra of bare ITO coated glass substrate is also measured for comparison. Strong peaks observed in the XRD of ITO are assigned to the (222), (400), (440), and (622) diffraction peaks of tin oxide (JCPDS:71-2194) [62]. The absence of

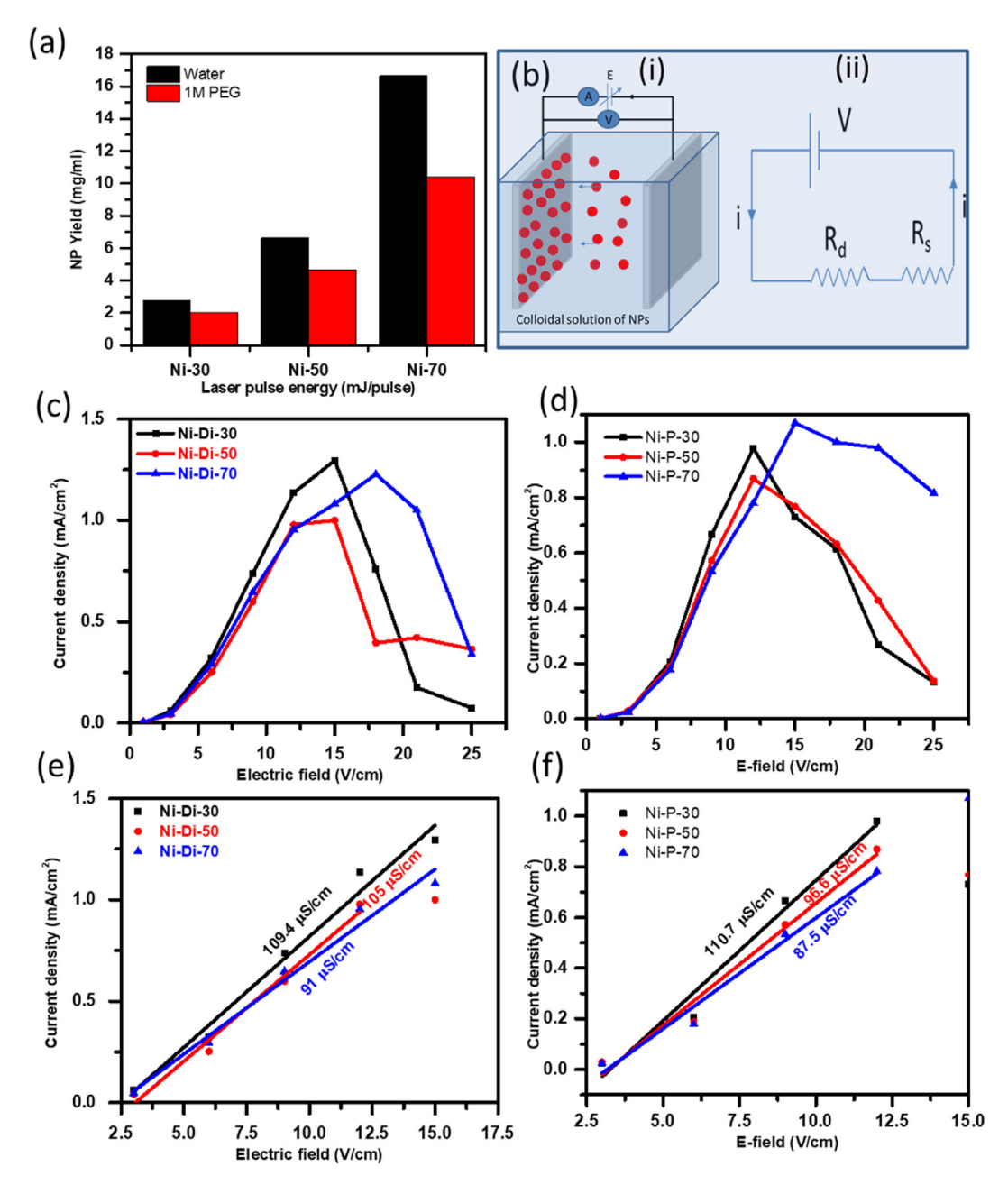


Fig. 3. (a) The yield of NPs through laser ablation of Ni target in distilled water and the aqueous media of PEG, (b) (i) schematic of the conductivity measurements of the colloidal solution of NPs and (ii) equivalent circuit of electrophoretic deposition. The current density (j) vs. electric field curves of the colloidal solutions of NPs produced in (c) distilled water and (d) in 1M aqueous media of PEG. The linear fitting of current density vs. electric field curve to get conductivity (σ) of different colloidal solution of NPs produced (e) distilled water and (f) aqueous media of PEG. NP, nanoparticle; PEG, polyethylene glycol.

tin oxide diffraction peaks in the samples deposited on the ITO coated glass substrate shows that the thickness of the sample is higher than the penetration depth of the X-ray beam. From the XRD investigation, we can see that Ni and NiO are dominant phases in the sample Ni-Di-70, while Ni and nickel hydroxide hydrate are dominant phases in the Ni-P-30 sample [63–66]. Nickel oxyhydroxide phase is also present in the sample prepared in the PEG water mixture. Observation of higher density of NiO in Ni-DI-70 sample shows that higher laser pulse energy establishes thermodynamic conditions for high temperature, high density, and high pressure (HTHDHP) for LPP and plasma-induced plasma (PIP), containing $\rm H^+$ and $\rm OH^-$ species from liquid and intermixing of two plasmas at LPP-PIP interface to produced Ni(OH)2 or NiOOH NPs. The initial high temperature of the as-grown NPs determines their

hydrothermal transformation from $Ni(OH)_2$ to NiO following the reaction $Ni(OH)_2 \rightarrow NiO + H_2O$ [69]. Surface oxidation of the NPs suspended in the liquid media is another possibility for the formation of a thin layer of oxide on the metal surface during the aging process [67,68]. The crystallite sizes of NPs in Ni-P-30 and Ni-DI-70 samples, calculated from the XRD pattern using the Debye-Scherrer formula [70], are 12 nm and 18 nm, respectively.

3.3. Vibrational characterizations of surface chemistry using Raman spectroscopy

The vibrational frequencies of a chemical compound are unique and particularly sensitive to the local environment. Therefore, lattice vibrational modes can be used as a fingerprint to diagnose the

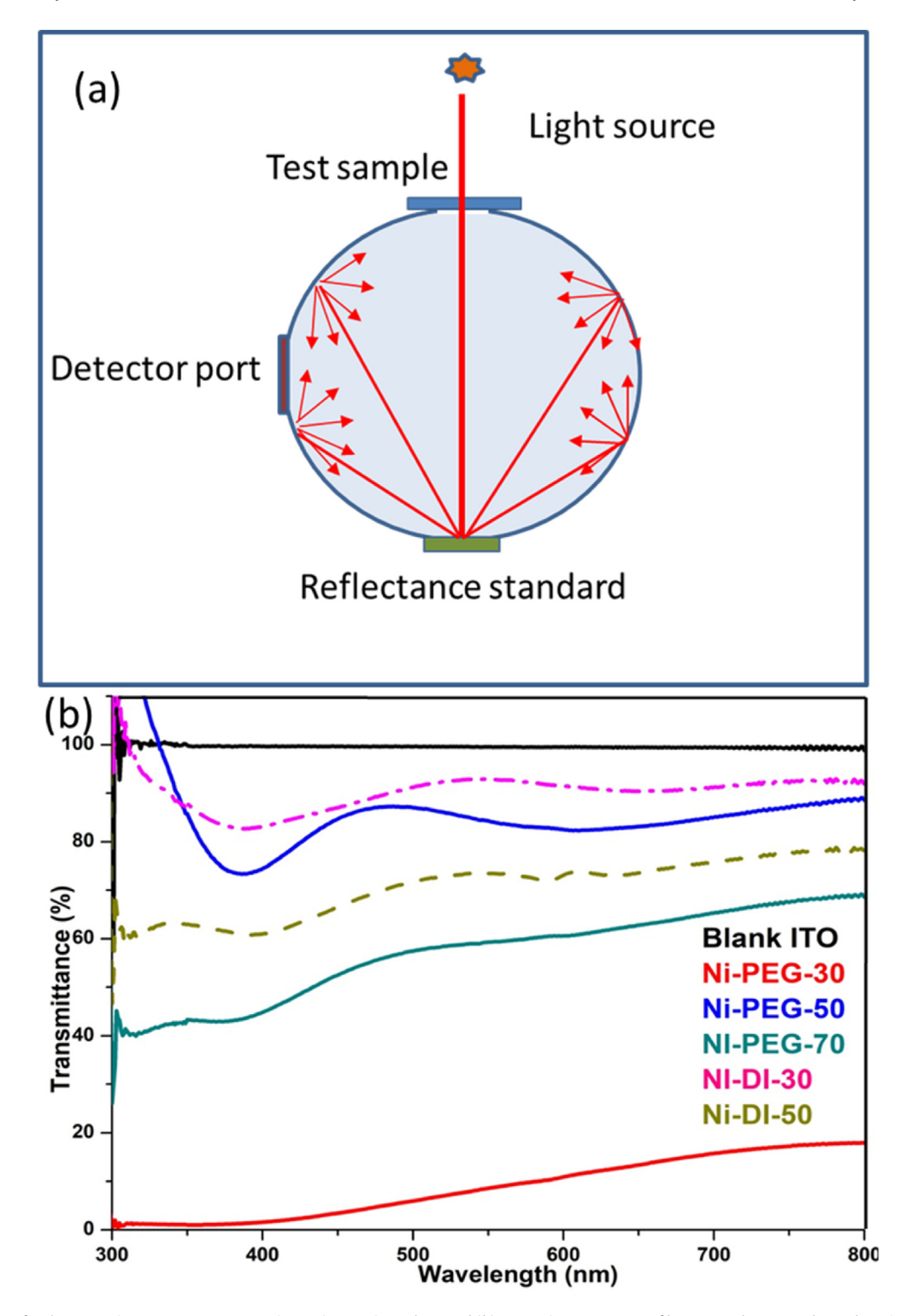


Fig. 4. (a) Ray diagram for the transmittance measurement using an integrating sphere and (b) Transmittance spectra of bare ITO substrate and EPD deposited Ni/NiO/Ni(OH)₂ NPs produced under different experimental conditions at ITO substrate. EPD, electrophoretic deposition; ITO, indium tin oxide; NP, nanoparticle.

surface chemistry of NPs. The Raman spectra of different samples deposited on ITO coated glass substrate are shown in Fig. 6(a) and (b). The two strong vibrational modes at frequencies 489 cm⁻¹ and 564 cm⁻¹ can be attributed to the symmetric stretching of Ni and OH bond in Ni(OH)₂. A strong peak in the frequency range of 1075–1085 cm⁻¹ is related to the two-magnon (2LO) transition of NiO [71–73]. Other vibrational modes at frequencies 770 cm⁻¹,

863 cm⁻¹, 1167 cm⁻¹, 1308 cm⁻¹, 1417 cm⁻¹, 1569 cm⁻¹, 1788 cm⁻¹, and 1906 cm⁻¹ are related to different Raman-active vibrational mode of different phases of Ni(OH)₂ [74]. The Raman spectra of samples produced in the aqueous media of PEG show a decrease in the relative intensity of the 2LO, NiO band, while an increase in the populations of OH-related bands with an increase in the laser pulse energy. These results show a decrease in the Ni/NiO ratio and an

Table 1Represents length, width and area of NPs deposited on ITO coated glass substrate.

S.No.	Sample	Length (cm)	Width (cm)	Area (cm²)
1.	Ni-DI-30	1.0	0.5	0.50
2.	Ni-DI-50	0.8	0.5	0.40
3.	Ni-DI-70	1.0	0.5	0.50
4.	Ni-P-30	1.6	0.5	0.80
5.	Ni-P-50	1.7	0.5	0.85
6.	Ni-P-70	1.3	0.5	0.65

increase in the $Ni(OH)_2$ and NiOOH phases in the samples produced in aqueous media of PEG at higher laser pulse energies. The variation in the frequencies of about $4-5~\rm cm^{-1}$ is due to surface defects, and vacancies present in the NPs are due to highly non-equilibrium processing associated with the laser ablation in the liquid for NPs generation [45]. The results of measurements confirm that nickel oxide/hydroxide and oxyhydroxide phases are present in all the samples that support our XRD investigations.

3.4. Size and surface morphological investigation using SEM

Surface morphology and nano/micro patterns on the surface of deposited film can give information regarding the size of particles, their tendency to form larger size aggregates/self-assembled structures on the electrode surface, and the role of the liquid molecules in the self-assembly. The scanning electron microscopy (SEM) images, elemental composition, and energy dispersive X-ray (EDX) spectra of NPs electrophoretically deposited from the corresponding colloidal solution produced in the aqueous medium of PEG are presented in Fig. 7. The sample produced at lower laser pulse energy (Ni-P-30) has 50–100 nm spheroidal aggregates (left

panel of Fig. 7(a)) on the surface of larger-sized islands with flat surfaces. From the comparatively smoother surface topography and dense organization pattern of these islands (Middle panel of Fig. 7(a)), one can say that these structures are formed with selfassembly of finer (5–10 nm) NPs. The high density of these structures is also supported by very low (<5-20%) hemispherical transmission. Nanostructured samples deposited from the solution produced with higher laser pulse energies (Fig. 7(b) and (c)) have higher corrugated patterns where surface roughness, size of structures formed, and degree of corrugation get increased with the laser pulse energy. For example, the surface of the sample Ni-P-50 has spheroidal particles of 100-200 nm, while sample Ni-P-70 has a two-dimensional sheet-like and elongated structure with a size in the range of 200-600 nm. The larger aggregates reduce packing density and may allow enhanced direct or scattered transmission of light through the spacing between the aggregates (Fig. 3). Corresponding elemental compositions are presented as bar graphs in the right panel of Fig. 7 and as EDX spectra in Fig. 7(d). The oxygen contents are higher in the samples Ni-P-30 (Ni/O: 0.17) and Ni-O-70 (Ni/O: 0.17) over the sample Ni-P-50 (Ni/O: 0.91). The higher oxygen content in the Ni-P-30 sample is possibly due to their smaller particle size i.e. a higher surface to volume ratio resulting in surface oxidation. In contrast, the higher oxygen content in larger size Ni-P-70 NPs, produced at a higher laser pulse energy, is possibly due to the generation of water plasma in front of the LPP plume and intermixing of these two plasmas before the nucleation and growth of the particles.

In contrast to the surface morphology of film electrophoretically deposited from aqueous media of PEG where NPs get assembled on the electrode to form large assemblies and islands, films deposited from the NPs solutions produced in water have isolated spherical

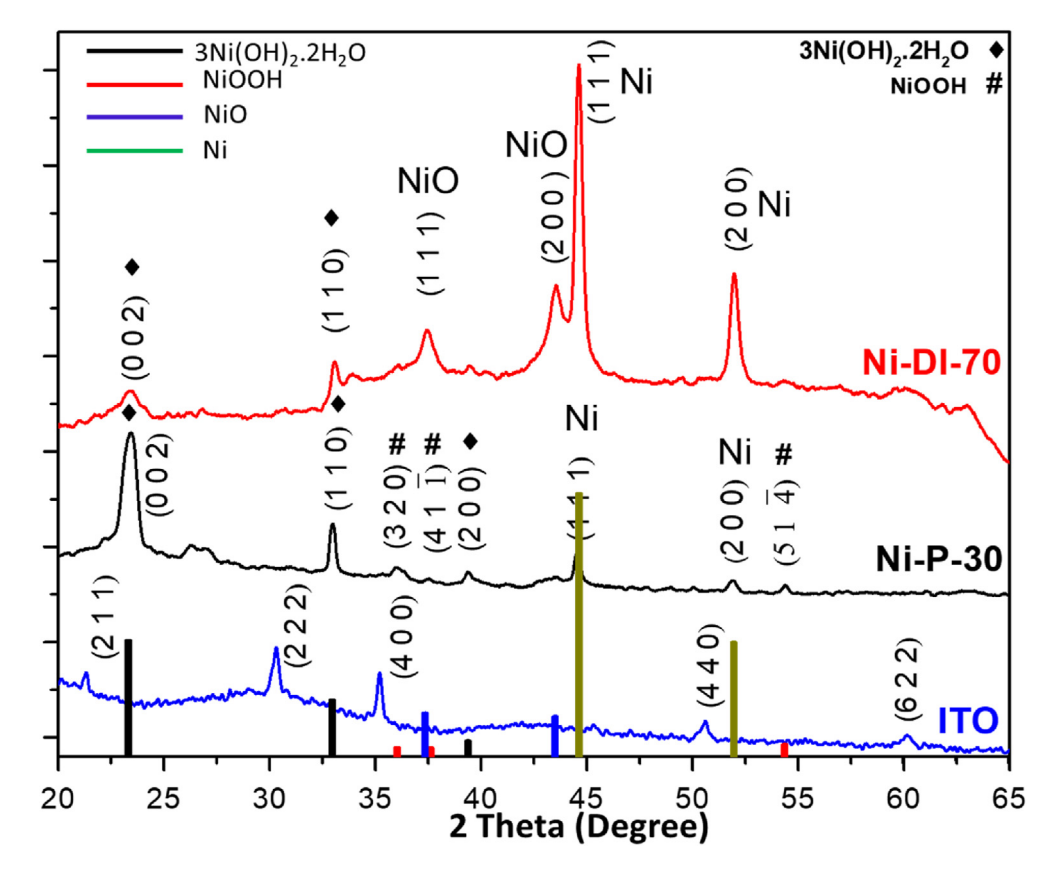


Fig. 5. X-ray diffraction spectra of nickel Ni/NiO/Ni(OH)₂ NPs deposited in ITO substrate from colloidal solutions Ni-Di-70 and Ni-P-30 NPs.The vertical lines show standard diffraction peaks of 3Ni(OH)₂₋₂H₂O (black), NiOOH(red), NiO(blue), and Ni (green). NP, nanoparticle.

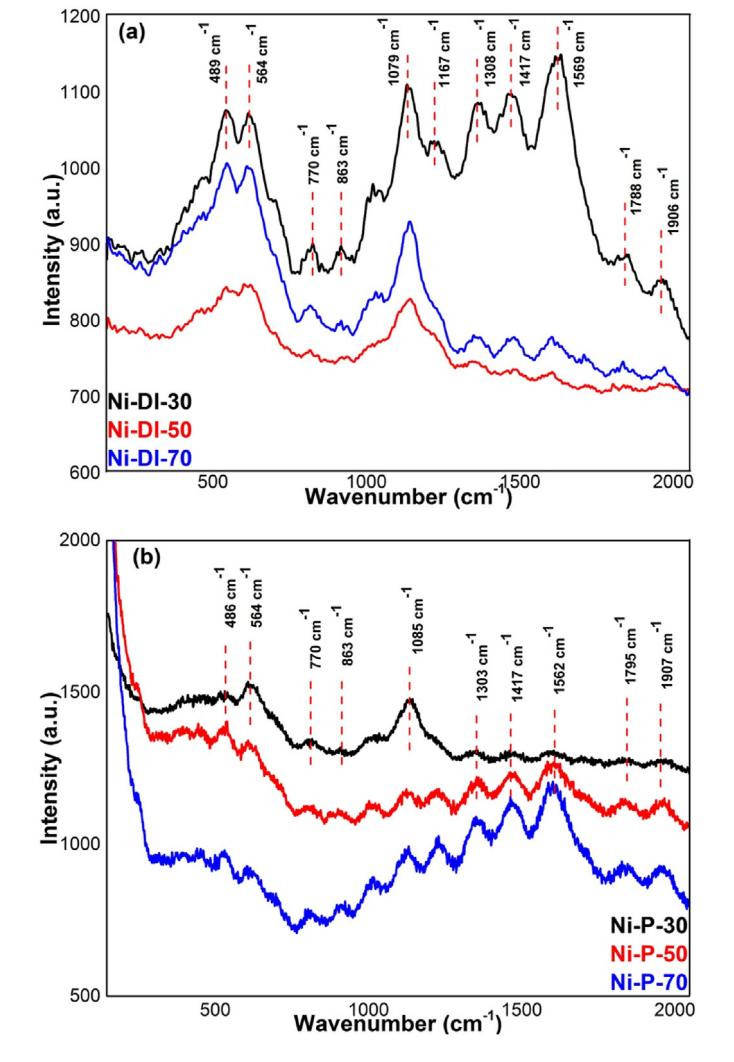


Fig. 6. Raman spectra of Ni/NiO/Ni(OH) $_2$ nanocomposite dielectrophoretic deposited from laser produced colloidal (**a**) in pure DI and (**b**) in aqueous media of 1 M PEG at different laser pulse energies. PEG, polyethylene glycol.

NPs (SEM image Fig. 8). In the case of water, NPs produced in the solution retain their identity when deposited on the substrate. The film deposited from solution produced at the lower laser pulse energy (Ni-Di-30) has well isolated monodispersed NPs in the size range of 5-20 nm (Fig. 8(a)). At a higher laser pulse energy (Ni-Di-50) tri-modal distribution of NPs in the size range of 5-20 nm, 40-80 nm, and 100-300 nm are observed in the deposited film. The larger sized, 40-80 nm, and 100-300 nm, spherical balls possibly get formed through the deposition of finer NPs on the surface of the cavitation bubble produced because of laser-induced water evaporation at the solid-water interface, as reported previously [47]. Laser ablation of a solid target at the solid-liquid interface, as in the present case, creates an air bubble, made of H₂O vapor or O₂ and H₂ gases, through laser-induced thermal dissociation of water. A bubble rapidly expands up to the largest size and then collapses. These bubbles trap surrounding NPs on their surface to reduce their surface energy and generally helps in the formation of larger-sized hollow spherical NPs [47]. The film deposited from the colloidal solution of NPs produced at 70 mJ/pulse energy (Ni-Di-70) has comparatively smaller sized, 5–20 nm, NPs than the film Ni-Di-50. In all three cases, the sizes of the abundance of intrinsic NPs are in the range of 5–20 nm. From the careful investigation of SEM images, we can conclude that PEG molecules act as linker molecules between NPs to expedite their self-assembly to make larger size clusters and aggregates. The high values of polarizability and dipole moment of PEG molecule are helpful in the building of electric field-controlled nano assembly [75]. The chemical composition of the NPs produced in pure water follows the same trend as that produced in the water/PEG mixture. For example, the smaller size of NPs in Ni-Di-30 (Ni/O: 0.28) and Ni-Di-70 (Ni/O: 0.39) have higher oxygen contents, while the NPs in the sample N-Di-50 are oxygen-deficient (Ni/O: 1.44) (Fig. 8(d)).

3.5. Electrochemical measurements

3.5.1. OER of different electrophoretically deposited working electrodes

The electrocatalytic performance of electrophoretically deposited nickel oxide/hydroxide NPs on ITO coated glass substrate was studied using LSV, EIS, and ECSA measurements using a standard three-electrode system in an alkaline (1M KOH) electrolyte. The working electrodes were pre-stabilized for 30-60 CV cycles with the scan rate of 20 mV/s before the measurement of LSV and EIS curves (supplementary information Fig. S1). The electrocatalysts synthesized in DI water are quite more stable than the samples synthesized in PEG solution. The OER polarization curves for working electrodes made with NiO/Ni(OH)₂ NPs samples produced in water and aqueous media of PEG are shown in Fig. 8(a) and (c). respectively. For a given laser pulse energy, the samples produced in the water show 10^2 - 10^3 times higher current density than the corresponding sample produced in the aqueous media of PEG. The onset potentials (η^1 ; potential at which current density >1 mA/ cm²) for samples Ni-Di-30, Ni-Di-50, and Ni-Di-70 are 1.630, 1.614, and 1.609 V (vs. RHE), respectively, and corresponding overpotentials (η^{10} ; potential at which current density ≥ 10 mA/cm²) are 2.158, 2.058, and 2.017 V (vs. RHE). The Tafel slope is a useful parameter to evaluate the electrocatalysis performance and provides information about the mechanism responsible for HER and OER processes. A smaller value of the Tafel slope determines the better performance of electrocatalyst is HER, as well as in OER. The linear portion of Tafel plots (Overpotential vs. Log (current density)) for different electrocatalysts samples (Fig. 9 (b) and (d) for samples produced in water and aqueous media of PEG, respectively) are fitted to the Tafel equation ($\eta = blog j + a$; where η is overpotential, j is current density, and b is the Tafel slope) to obtain corresponding Tafel slope. The Tafel slope of Ni-Di-70 (72.6 mV/dec) is significantly lower than the Ni-Di-50 (78.5 mV/dec) and Ni-Di-30 (84.8 mV/dec) samples produced at lower laser pulse energies. The Tafel slopes of electrocatalysts produced in aqueous media of PEG are much higher 330 mV/dec for Ni-P-30, 320 mV/dec for Ni-P-50, and 250 mV/dec for Ni-P-70 (Fig. 9(d)). The EIS of electrocatalysts, produced by PLA in water (Fig. 9(e)) shows significantly lower charge transfer resistance for Ni-Di-70 (24 k Ω) over Ni-Di-50 (48.5 k Ω) and Ni-Di-30 (176 k Ω). To understand the effect of loading on the OER performance, we loaded 0.5, 1.0, and 2.0 mg of Ni-Di-70 electrocatalyst on ITO coated glass substrate and recorded their OER polarization curves (supporting information Fig. S2)). At lower potentials (E < 2.75 V vs. RHE), the OER current density is inversely proportional to the catalyst loading. However, at potentials larger than 2.75 V, the OER performance is proportional to the loading. The observed results demonstrate that at lower potentials the OH⁻ ions get adsorbed only at the surface and edges of the top layer of the EPD film. Two mg of Ni-Di-70 electrocatalyst power was electrophoretically loaded on a 1cm × 1 cm Ni-foam (NF) substrate for chronopotentiometry (CP) test to demonstrate stability and durability. As can be seen from the CP curves of the Ni-Di-70@NF and the bare NF substrate, the required voltage (E vs. RHE) to produce

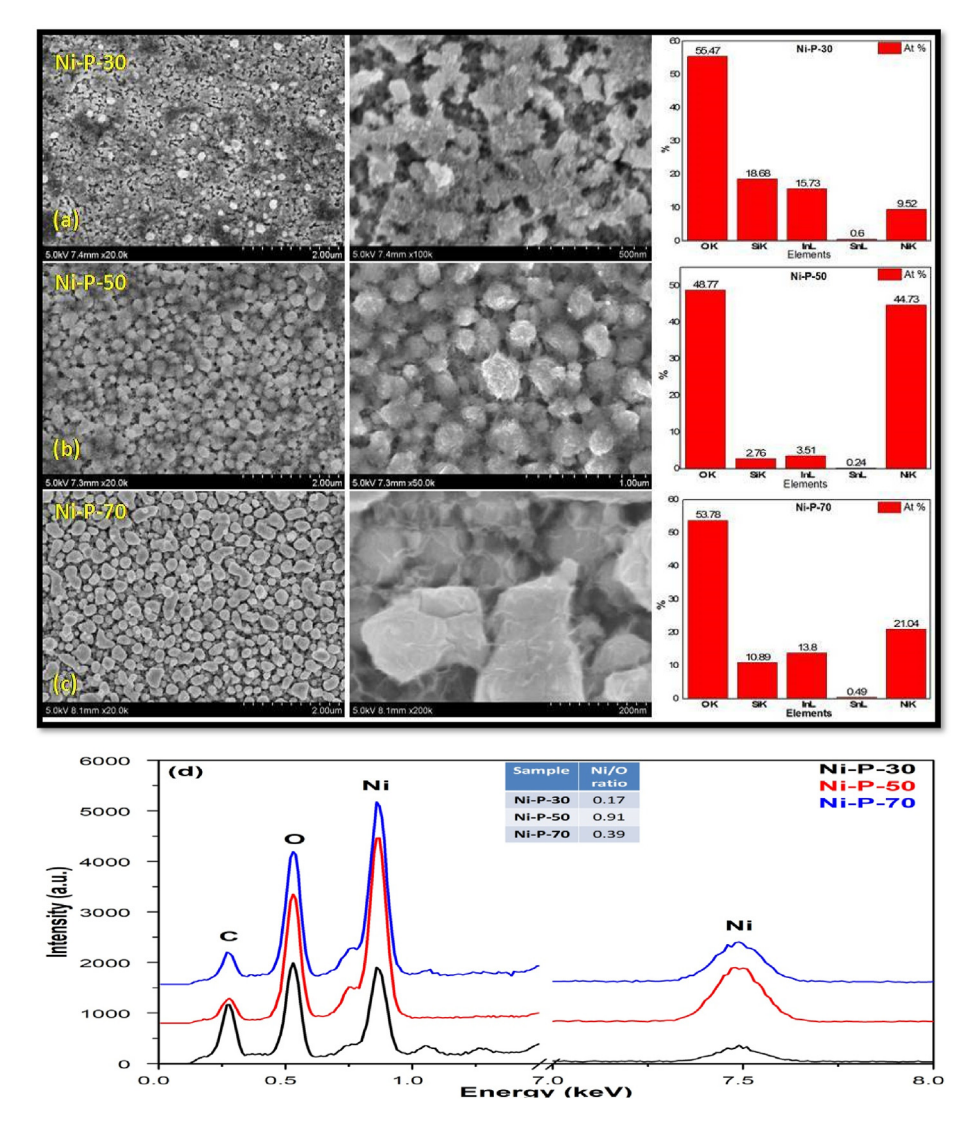


Fig. 7. SEM images of Ni/NiO/Ni(OH)₂ NPs dielectrophoretic deposited on ITO coated glass slide from the PLA produced colloidal solutions (a) Ni-P-30, (b) Ni-P-50, and (c) Ni-P-70. The right panel shows the corresponding elemental composition measured from EDX in % Atom (red), and (d) corresponding EDAX spectra.

10 mA/cm² is changed by only 3 mA (0.9%) for the Ni-Di-70@NF system compared with 30 mA (9%) for the bare NF in 5 h. Thus, the produced electrocatalyst has 10 times higher stability and durability than its substrate. The double-layer capacitance ($C_{\rm dl}$) values, estimated from the corresponding CV measurements in the non-Faradaic potential region (supporting information Fig. S3 and S4), of Ni-Di-70 (6.53 \times 10 $^{-4}$ mF/cm²) electrocatalyst and bare ITO coated glass substrate (1.46 \times 10 $^{-4}$ mF/cm²) show \sim 45 times increase in the ECSA. The high OER performance of Ni-Di-70 electrocatalyst is possibly due to the synergistic effect of increased ECSA (extrinsic) and higher content of NiO (intrinsic activity) in the sample.

3.5.2. HER of different electrophoretically deposited working electrodes

The HER polarization curves for different working electrodes prepared from the colloidal solutions of NPs produced in distilled water and aqueous media of PEG are presented in Fig. 10(a) and (c), respectively. The HER polarization curve of bare ITO coated glass substrate is also presented as a reference. Very similar to the OER results, HER polarization curves for electrocatalysts obtained from PLA in water have two to three orders (~10²-10³) times higher

current density over the corresponding material produced in the aqueous media of PEG. The onset potentials (η^1) for electrocatalysts Ni-Di-30, Ni-Di-50, and Ni-Di-70 are 416, 325, and 64 mV, respectively. Much lower onset potential for Ni-Di-70 may be due to a higher ratio of NiO/Ni in as produced NPs. Similarly, overpotential, η¹⁰, for water-produced electrocatalysts are 866, 689, and 277 mV (Table 2). The EIS measurements of electrocatalysts produced in water (Fig. 10(b)) show significantly lower charge transfer resistance for Ni-Di-70 (2.3 k Ω) over Ni-Di-50 (21 k Ω) and Ni-Di-30 (42 $k\Omega$). Similarly, the charge transfer resistance for Ni-P-70 (600 $k\Omega$) electrocatalyst is lower than that of the Ni-P-70 (7.5 M Ω). From these results, we can say that the charge transfer resistance of electrocatalysts produced in PEG is 10²-10³ times higher than the corresponding samples produced in distilled water. The Tafel plots of different samples presented in Fig. 9(e) show that Ni-Di-70 (Tafel slope 98 mV/dec) is the best, while Ni-P-30 (Tafel slope 950 mV/dec) is the worse HER performer. The chronopotentiometry (CP) measurement of the best HER performer. Ni-Di-70, at 20 μA/cm², 2 mA/cm², and 20 mA/cm² current densities with quite stable potential values show stability and durability of the electrocatalyst in the alkaline medium. Almost the same value of $C_{\rm dl}$ for Ni-Di-70 (7.3 \times 10⁻⁵ mF/cm²) electrocatalyst and bare ITO

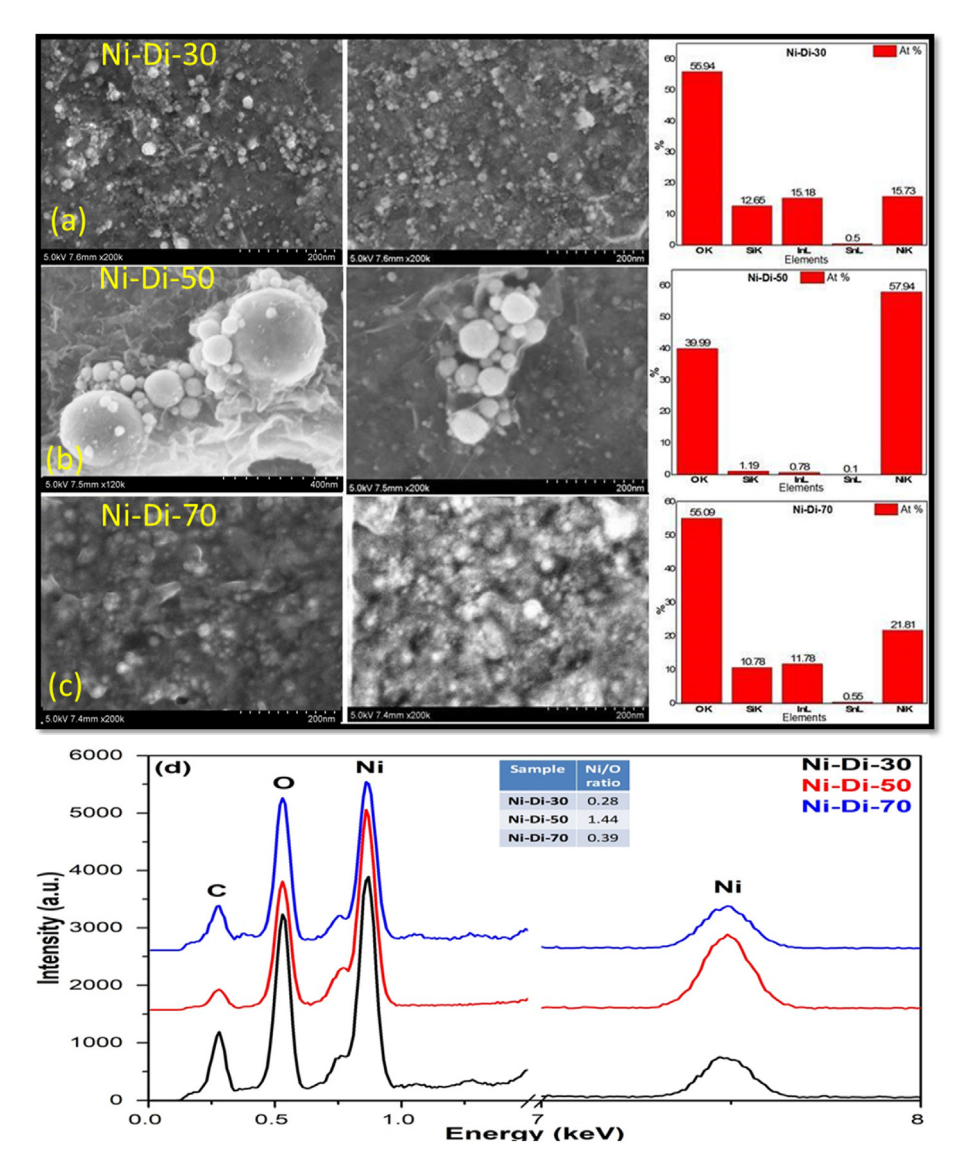


Fig. 8. SEM images of NiO/Ni(OH)₂ NPs dielectrophoretic deposited on ITO coated glass slide from the PLA produced colloidal solutions (**a**) Ni-Dl-30, (**b**) Ni-Dl-50, and (**c**) Ni-Dl-70. The right panel shows the corresponding elemental composition measured from EDX in % Atom (red), and (**d**) corresponding EDAX spectra. ITO, indium tin oxide; NP, nanoparticle; SEM, scanning electron microscopy.

coated glass substrate (7.48 \times 10⁻⁵ mF/cm²), as shown in supporting information Fig. S4 (a) and (c), shows their equal ECSA responsible for the HER activity. Almost 43 times larger current density (at 0.5 V vs. RHE) from Ni-Di-70 electrocatalysts over bare ITO coated glass substrate from almost the same value of ECSA shows excellent intrinsic HER activity of Ni/NiO interface present in the electrocatalyst. To understand the effect of loading on the HER performance, we loaded 0.5, 1.0, and 2.0 mg of Ni-Di-70 electrocatalyst on ITO coated glass substrate and recorded their HER polarization curves (supporting information Fig. S5)). In contrast to the OER, the HER performance increases with the loading at all potentials and the effect of loading is more significant at a higher potential. The SEM image and EDAX spectrum (Fig. S6) recorded after the electrochemical measurements demonstrate strong adhesion of the particle to the substrate and an increase in the oxygen content over time.

As can be seen from XRD and Raman investigations that samples prepared in distilled water at higher laser pulse energy have Ni/NiO phase in dominance, while samples prepared either in aqueous media of PEG or at lower laser pulse energy in water have an abundance of Ni/Ni(OH)₂ phase. It is widely known that interfaces of Ni and NiO have high electrocatalytic water splitting performance where NiO get reduced into NiOOH through the following reversible reaction $NiO + OH^- = NiOOH + e^-$ [76–80]. As reported previously, higher electrocatalytic performance for Ni/NiO samples may be due to the presence of neutral nickel, Ni(0), at the interface of Ni and NiO [81], with low Gibbs free energy (ΔG_{H^*}) for H* adsorption. Here Ni(0) sites attract and adsorb H*, while neighboring NiO sites attract OH* to split water molecules comparatively at lower overpotential [82]. Much lower electrocatalytic performance of electrocatalysts produced in aqueous media of PEG is possibly due to the combined effect of synthesis of Ni/Ni(OH) 2 or

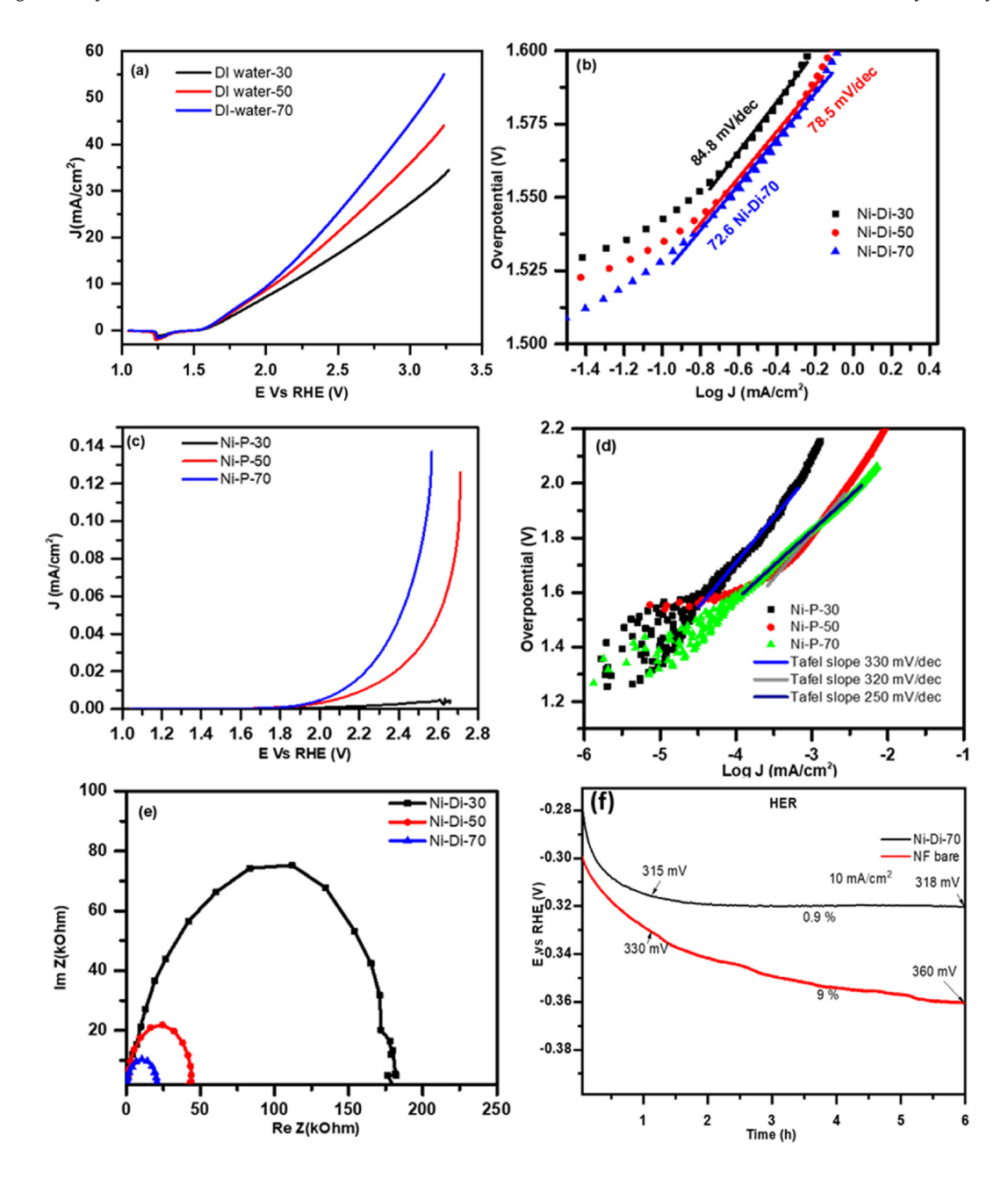


Fig. 9. Oxygen evolution reaction (OER) (a) and (c) polarization curves and (b) and (d) Tafel plots for Ni/NiO/Ni(OH)₂ NPs electrophoretic deposited on ITO coated glass slides from PLA produced a colloidal solution in (a) distilled water and (c) in 1M solution of PEG in water. (e) Electrochemical impedance spectra of electrocatalysts produced by PLA in water with different laser pulse energies biased at dc potential 1.54 V (RHE) superimposed with 10 mV of ac signal from 0.001 HZ to 1MHz. (f) The chronopotentiometry (CP) curve against OER for Ni-Di-70 (black curve) and bare Ni-foam at 10 mA/cm² current density for 6 h. ITO, indium tin oxide; NP, nanoparticle; PEG, polyethylene glycol.

Ni/NiOOH, having lower activity over Ni/NiO phases, and adsorption of the residue of PEG or its fragments on the active sites.

For HER, Volmer-Tafel (equation (1)), as well as Volmer-Heyrovsky (equation (2)) pathways, involve (i) adsorption of H_2O molecule on electrocatalysts, (ii) electrochemical reduction of adsorbed H_2O into adsorbed H atom and OH^- , and (iii) desorption of OH^- ion and synthesis of another H adsorbed atom to generate hydrogen through following equations:

$$H_2O + e \rightarrow H_{ads} + OH^-$$
 (Volmer)
 $H_{ads} + H_{ads} \rightarrow H_2$ (Tafel)

$$H_2O + e \rightarrow H_{ads} + OH^-$$
 (Volmer)

$$H_2O + H_{ads} + e \rightarrow H_2 + OH^-$$
 (2)

At Ni/NiO interface, hydrogen atoms produced through water splitting preferentially get adsorbed at the Ni site because of its similarity with Pt for H atom adsorption [82,83], while the strong electrostatic affinity of positively charged Ni⁺² species at neighboring NiO sites offers adsorption sites for OH⁻ ions to accomplish Volmer process. In this way, the electrocatalytic process synergistically occurs at Ni/NiO interface. Lower electrocatalytic activity of samples produced in aqueous media of PEG may be due to the adsorption of PEG molecules and hence blockage of active sites. This can be verified by the absence of redox peaks in the CV cycles of the PEG-produced electrocatalysts (Supplementary information Fig. S1).

(1)

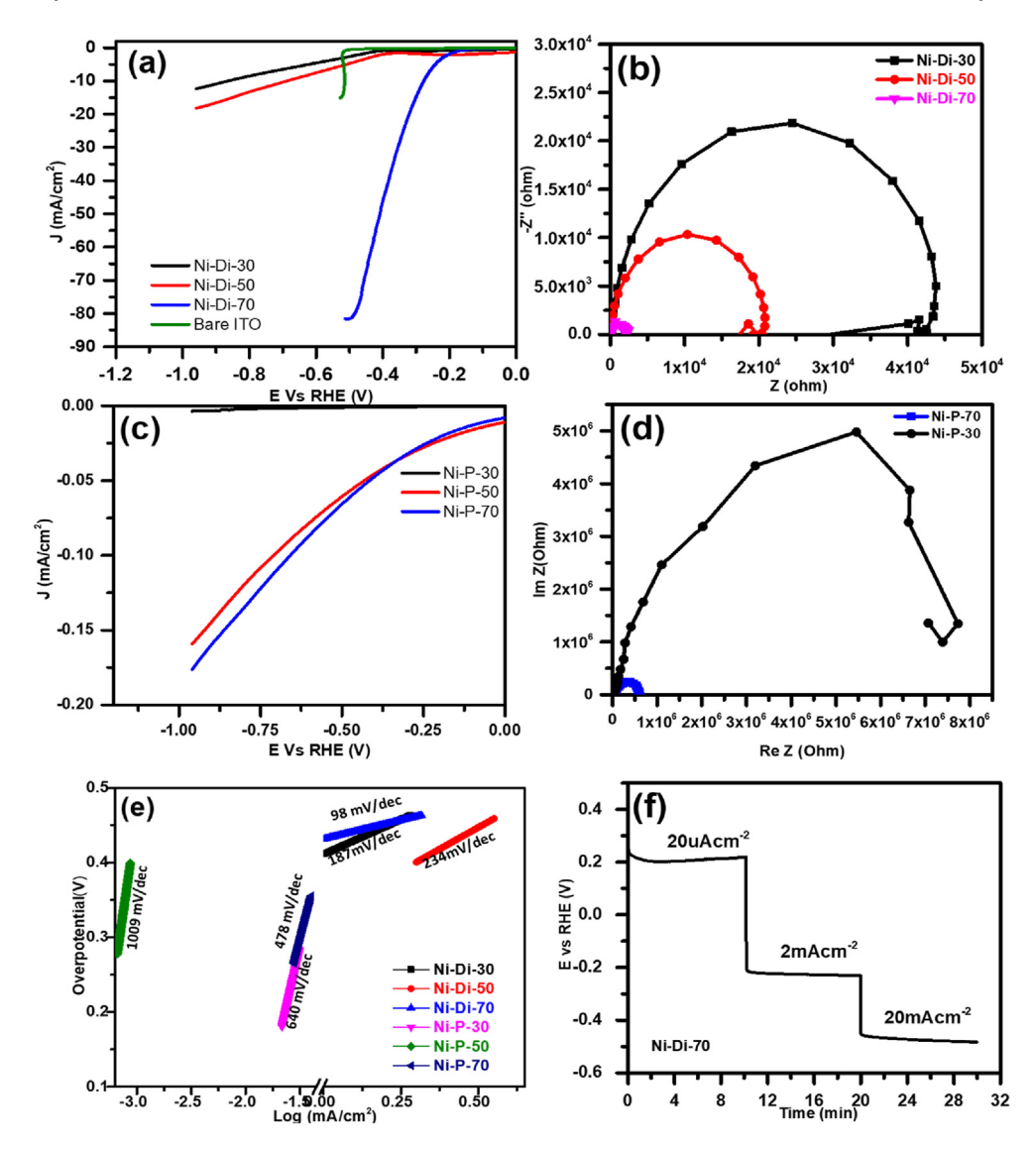


Fig. 10. Hydrogen evolution reaction (HER) (a) and (c) polarization curves and (b) and (d) corresponding EIS curves for Ni/NiO/Ni(OH)₂ electrocatalysts electrophoretically deposited on ITO coated glass slides from different PLA produced a colloidal solution in (a) and (b) distilled water and (c) and (d) in 1 M aqueous solution of PEG. Polarization curve of bare ITO (green curve) is also provided for reference (e) The Tafel slopes of different electrocatalyst materials, and (f) Chronopotentiometry measurement for the best electrocatalyst, Ni-Di-70, at current densities + 20 μ A/cm², 2 mA/cm², and 20 mA/cm² for 30 min. EIS, electrochemical impedance spectroscopy; ITO, indium tin oxide; PEG, polyethylene glycol.

Table 2Summary of HER/OER parameters of different Ni/NiO/Ni(OH)₂ electrocatalysts samples.

Sample	HER				OER		
	$\eta^1 (\text{mV})$	η ¹⁰ (mV)	EIS R_{ct} ($k\Omega$)	Tafel slope (mV/dec)	$\eta^1 (mV)$	η ¹⁰ (mV)	Tafel slope (mV/dec)
Ni-Di-30	416	866	42	218	1630	2158	84.8
Ni-Di-50	325	689	21	101	1614	2058	78.5
Ni-Di-70	64	277	2.3	98	1609	2017	72.6
Ni-P-30	_	_	7500	950	_	_	330
Ni-P-50	_	_	_	438	_	_	320
Ni-P-70	_	_	600	150	_	_	250

4. Conclusion

In summary, we report PLA in liquid in combination with ex-situ EPD for the fabrication of ready-to-use $Ni/NiO/Ni(OH)_2$ electrocatalyst substrates for overall water splitting. PLA of nickel target at three different laser pulse energies in distilled water or aqueous media of 1M PEG was performed to produce six sets of colloidal

solutions of NPs followed by ex-situ EPD to make six electrocatalysts. From the XRD and Raman investigations, we observed that the electrocatalyst samples produced in the water at higher laser pulse energies have Ni/NiO phase in abundance, while the samples produced at any energy in aqueous media of PEG or lower laser pulse energy in water dominate Ni/Ni(OH)₂/NiOOH phases. Among all electrophoretically deposited samples, Ni-Di-70 is the best

performer in overall water splitting, while Ni-P-30 is the worse. We believe that metallic Ni(0) sites of Ni/NiO attract and adsorbs H* while neighboring NiO sites attract OH* to effectively split water molecules comparatively at lower overpotential. The poor performance of all PEG-produced electrocatalysts is possibly due to the formation of larger assembly through PEG molecules assisted linkage among NPs that reduces the overall electrochemical active surface area. The available active sites may get further blocked because of the adsorption of PEG molecules or residue of their laser fragments on the surface of Ni/Ni(OH)₂/NiOOH that reduces their intrinsic electrocatalytic activities. The present work explores the possibility of PLA in liquids for the synthesis of a range of catalyst NPs, beyond Nibased materials, with surfaces free from contamination and EPD of these NPs on the desired substrate to make ready-to-use electrocatalysts for a wealth of chemical reactions.

Credit author statement

S.C.S. and A.S. came with the idea and designed the project. A.S. and C.S.S. performed most of the experiments. S.C.S and AS analyzed the data and GV helped in some calculations. AS initially organized the figures and scientific content and S.C.S. prepared and finalized the manuscript with C.G. SCS revised the manuscript and addressed reviewers' comments.

Data availability

The raw/processed data required to reproduce these findings cannot be shared at this time due to technical or time limitations.

Declaration of competing interest

The authors declare that they have no known competing financial interests or personal relationships that could have appeared to influence the work reported in this article.

Acknowledgments

We acknowledge financial supports from the Bill & Melinda Gates Foundation (OPP1157723), the National Basic R&D program of China (2018YFB1107202), National Natural Science Foundation of China (11774340); Scientific Research Project of the Chinese Academy of Sciences (QYZDB-SSW-SYS038), Jilin Province Science & Technology Development Project (20180414019GH), and K.C. Wong Education Foundation (G[TD-2018-08).

Appendix A. Supplementary data

Supplementary data to this article can be found online at https://doi.org/10.1016/j.mtchem.2021.100691.

References

- G. Zhao, K. Rui, S.X. Dou, W. Sun, Heterostructures for electrochemical hydrogen evolution reaction: a review. Adv. Funct. Mater. 28 (2018) 1803291.
- [2] Z. Cai, X. Bu, P. Wang, J.C. Ho, J. Yang, X. Wang, Recent advances in layered double hydroxide electrocatalysts for the oxygen evolution reaction, J. Mater. Chem. A. 7 (2019) 5069.
- [3] N. Dubouis, A. Grimaud, The hydrogen evolution reaction: from material to interfacial descriptors, Chem. Sci. 10 (2019) 9165.
- [4] (a) S. Anantharaj, S.R. Ede, K. Karthick, S.S. Sankar, K. Sangeetha, P.E. Karthik, S. Kundu, Precision and correctness in the evaluation of electrocatalytic water splitting: revisiting activity parameters with a critical assessment, Energy Environ. Sci. 11 (2018) 744–771;
 - (b) Z. Li, S.A. Jalil, S.C. Singh, W. Li, X. Wei, C. Guo, Significantly enhanced electrocatalytic activity of copper for hydrogen evolution reaction through femtosecond laser blackening, Int. J. Hydrogen Energy 46 (2021) 10783–10788.

- [5] E. Willinger, C. Massué, R. Schlögl, M.G. Willinger, Identifying key structural features of IrOxWater splitting catalysts, J. Am. Chem. Soc. 139 (2017) 12093–12101.
- [6] J. Shan, T. Ling, K. Davey, Y. Zheng, S. Qiao, Transition-metal-doped Rulr bifunctional nanocrystals for overall water splitting in acidic environments, Adv. Mater. 31 (2019) 1900510.
- [7] D. Liu, X. Li, S. Chen, H. Yan, C. Wang, C. Wu, Y.A. Haleem, S. Duan, J. Lu, B. Ge, P.M. Ajayan, Y. Luo, J. Jiang, L. Song, Atomically dispersed platinum supported on curved carbon supports for efficient electrocatalytic hydrogen evolution, Nat Energy 4 (2019) 512–518.
- [8] N. Cheng, S. Stambula, D. Wang, M.N. Banis, J. Liu, A. Riese, B. Xiao, R. Li, T. Sham, L. Liu, G.A. Botton, X. Sun, Platinum single atom and cluster catalysis of the hydrogen evolution reaction, Nat. Commun. 7 (2016) 13638.
- [9] Z.W. Seh, J. Kibsgaard, C.F. Dickens, I. Chorkendorff, J.K. Nørskov, T.F. Jaramillo, Combining theory and experiment in electrocatalysis: insights into materials design, Science 355 (2017) 4998.
- [10] (a) B. Bayatsarmadi, Y. Zheng, A. Vasileff, S. Qiao, Recent Advances in Atomic Metal Doping of Carbon-Based Nanomaterials for Energy Conversion, Small 13 (2017) 1700191;
 (b) Chaudry S. Saraj, S.C. Singh, A. Shukla, W. Yu, M. Umer Fayyaz, C. Guo,

Single-step and sustainable fabrication of Ni (OH) 2/Ni foam water splitting catalysts via electric field assisted pulsed laser ablation in liquid, ChemElectroChem 8 (2021) 209–217.

- [11] B. Lai, S.C. Singh, J.K. Bindra, C.S. Saraj, A. Shukla, T.P. Yadav, W. Wu, S.A. McGill, N.S. Dalal, A. Srivastava, C. Guo, Hydrogen evolution reaction from bare and surface-functionalized few-layered MoS2 nanosheets in acidic and alkaline electrolytes, Mater. Today Chem. 14 (2019) 100207.
- [12] W. Yu, J. Yin, Y. Li, B. Lai, T. Jiang, Y. Li, H. Liu, J. Liu, C. Zhao, S.C. Singh, J. Chen, B. Lin, H. Idriss, C. Guo, Ag2S quantum dots as an infrared excited photocatalyst for hydrogen production, ACS Appl. Energy Mater. 2 (2019) 2751.
- [13] F.M. Pesci, M.S. Sokolikova, C. Grotta, P.C. Sherrell, F. Reale, K. Sharda, N. Ni, P. Palczynski, C. Mattevi, MoS2/WS2 heterojunction for photoelectrochemical water oxidation, ACS Catal. 7 (2017) 4990–4998.
- [14] U. Gupta, C.N.R. Rao, Hydrogen generation by water splitting using MoS2 and other transition metal dichalcogenides, Nano Energy 41 (2017) 49–65.
- [15] B. Liu, C. Kuo, J. Chen, Z. Luo, S. Thanneeru, W. Li, W. Song, S. Biswas, S.L. Suib, J. He, Ligand-assisted Co-assembly approach toward mesoporous hybrid catalysts of transition-metal oxides and noble metals: photochemical water splitting, Angew. Chem. Int. Ed. 54 (2015) 9061–9065.
- [16] Y. Wang, D. Yan, S.E. Hankari, Y. Zou, S. Wang, Recent progress on layered double hydroxides and their derivatives for electrocatalytic water splitting, Adv. Sci. 5 (2018) 1800064.
- [17] F.A.L. Laskowski, M.R. Nellist, J. Qiu, S.W. Boettcher, Metal oxide/(oxy)hy-droxide overlayers as hole collectors and oxygen-evolution catalysts on water-splitting photoanodes, J. Am. Chem. Soc. 141 (2019) 1394–1405.
- [18] F. Song, L. Bai, A. Moysiadou, S. Lee, C. Hu, L. Liardet, X. Hu, Transition metal oxides as electrocatalysts for the oxygen evolution reaction in alkaline solutions: an application-inspired renaissance, J. Am. Chem. Soc. 140 (2018) 7748–7759.
- [19] J. Jang, C. Du, Y. Ye, Y. Lin, X. Yao, J. Thorne, E. Liu, G. McMahon, J. Zhu, A. Javey, J. Guo, D. Wang, Enabling unassisted solar water splitting by iron oxide and silicon, Nat. Commun. 6 (2015) 7447.
- [20] X. Deng, H. Tüysüz, Cobalt-oxide-based materials as water oxidation catalyst: recent progress and challenges, ACS Catal. 4 (2014) 3701–3714.
- [21] J.-X. Feng, H. Xu, Y.-T. Dong, X.-F. Lu, Y.-X. Tong, G.-R. Li, Efficient hydrogen evolution electrocatalysis using cobalt nanotubes decorated with titanium dioxide nanodots, Angew. Chem. Int. Ed. 56 (2017) 2960.
- [22] H. Xu, Z.-X. Shi, Y.-X. Tong, G.-R. Li, Porous microrod arrays constructed by carbon-confined NiCo@NiCoO2 Core@Shell nanoparticles as efficient electrocatalysts for oxygen evolution, Adv. Mater. 30 (2018) 1705442.
- [23] A. Wang, H. Xu, G. Li, NiCoFe layered triple hydroxides with porous structures as high-performance electrocatalysts for overall water splitting, ACS Energy Lett 1 (2016) 445–453.
- [24] M.B. Stevens, C.D.M. Trang, L.J. Enman, J. Deng, S.W. Boettcher, Reactive Fesites in Ni/Fe (Oxy)hydroxide are responsible for exceptional oxygen electrocatalysis activity, J. Am. Chem. Soc. 139 (2017) 11361–11364.
- [25] M.S. Burke, L.J. Enman, A.S. Batchellor, S. Zou, S.W. Boettcher, Oxygen evolution reaction electrocatalysis on transition metal oxides and (Oxy)hydroxides: activity trends and design principles, Chem. Mater. 27 (2015) 7549—7558.
- [26] X. Long, Z. Wang, S. Xiao, Y. An, S. Yang, Transition metal based layered double hydroxides tailored for energy conversion and storage, Mater. Today 19 (2016) 213–226.
- [27] Q. Wang, D. O'Hare, Recent advances in the synthesis and application of layered double hydroxide (LDH) nanosheets, Chem. Rev. 112 (2012) 4124–4155.
- [28] C.-F. Li, J.-W. Zhao, L.-J. Xie, J.-Q. Wu, Q. Ren, Y. Wang, G.-R. Li, Surface-adsorbed carboxylate ligands on layered double hydroxides/metal—organic frameworks promote the electrocatalytic oxygen evolution reaction, Angew. Chem. Int. Ed. 60 (2021) 18129.
- [29] N. Han, P. Liu, J. Jiang, L. Ai, Z. Shao, S. Liu, Recent advances in nanostructured metal nitrides for water splitting, J. Mater. Chem. A. 6 (2018) 19912.
- [30] D.E. Schipper, Z. Zhao, H. Thirumalai, A.P. Leitner, S.L. Donaldson, A. Kumar, F. Qin, Z. Wang, L.C. Grabow, J. Bao, J. Bao, K.H. Whitmire, Effects of catalyst phase on the hydrogen evolution reaction of water splitting: preparation of phase-pure films of FeP, Fe2P, and Fe3P and their relative catalytic activities, Chem. Mater. 30 (2018) 3588—3598.

- [31] C.G. Read, J.F. Callejas, C.F. Holder, R.E. Schaak, General strategy for the synthesis of transition metal phosphide films for electrocatalytic hydrogen and oxygen evolution, ACS Appl. Mater. Interfaces 8 (2016) 12798–12803.
- [32] Y. Dang, J. He, T. Wu, L. Yu, P. Kerns, L. Wen, J. Ouyang, S.L. Suib, Constructing bifunctional 3D holey and ultrathin CoP nanosheets for efficient overall water splitting, ACS Appl. Mater. Interfaces 11 (33) (2019) 29879–29887.
- [33] S. Li, Xi Cong, Y. Jin, D. Wu, J. Wang, T. Liu, H. Wang, C. Dong, H. Liu, S.A. Kulinich, X. Du, Ir—O—V catalytic group in Ir-doped NiV(OH)2 for overall water splitting, ACS Energy Lett 4 (2019) 1823—1829.
- [34] L. Chen, X. Dong, Y. Wang, Y. Xia, Separating hydrogen and oxygen evolution in alkaline water electrolysis using nickel hydroxide, Nat. Commun. 7 (2016) 11741.
- [35] Q. Zhang, C. Zhang, J. Liang, P. Yin, Y. Tian, Orthorhombic α-NiOOH nanosheet arrays: phase conversion and efficient bifunctional electrocatalysts for full water splitting, ACS Sustain. Chem. Eng. 5 (2017) 3808–3818.
- [36] D. Wang, Q. Li, C. Han, Z. Xing, X. Yang, When NiO@Ni meets WS2 nanosheet array: a highly efficient and ultrastable electrocatalyst for overall water splitting, ACS Cent. Sci. 4 (2018) 112–119.
- [37] S. Guan, X. Fu, Z. Lao, C. Jin, Z. Peng, NiS—MoS2 hetero-nanosheet array electrocatalysts for efficient overall water splitting, Sustain. Energy Fuel. 3 (2019) 2056–2066.
- [38] X. Zheng, X. Han, Y. Zhang, J. Wang, C. Zhong, Y. Deng, W. Hu, Controllable synthesis of nickel sulfide nanocatalysts and their phase-dependent performance for overall water splitting, Nanoscale 11 (2019) 5646–5654.
- [39] J. Zhang, Y. Wang, C. Zhang, H. Gao, L. Lv, L. Han, Z. Zhang, Self-supported porous NiSe2 nanowrinkles as efficient bifunctional electrocatalysts for overall water splitting, ACS Sustain. Chem. Eng. 6 (2018) 2231–2239.
- [40] P.C. Ray, H. Yu, P.P. Fu, Toxicity and environmental risks of nanomaterials: challenges and future needs, J. Environ. Sci. Health C Environ. Carcinog. Ecotoxicol. Rev. 27 (1) (2009) 1–35.
- [41] V. Misra, S.D. Pandey, Hazardous waste, impact on health and environment for development of better waste management strategies in future in India, Environ, Int. 3 (2005) 417–431
- viron. Int. 3 (2005) 417–431.
 [42] (a) I. Hussain, N.B. Singh, A. Singh, H. Singh, S.C. Singh, Green synthesis of nanoparticles and its potential application, Biotechnol. Lett. 38 (4) (2016) 545–560:
 - (b) I. Hussain, N.B. Singh, A. Singh, H. Singh, S.C. Singh, V. Yadav, Exogenous application of phytosynthesized nanoceria to alleviate ferulic acid stress in Solanum lycopersicum, Scientia horticulturae 214 (2017) 158–164.
- [43] A.K. Bhardwaj, A. Shukla, S. Maurya, S.C. Singh, K.N. Uttam, S. Sundaram, M.P. Singh, R. Gopal, Direct sunlight enabled photo-biochemical synthesis of silver nanoparticles and their Bactericidal Efficacy: photon energy as key for size and distribution control, J. Photochem. Photobiol. B Biol. 188 (2018) 42–49.
- [44] D. Zhang, B. Gökce, S. Barcikowski, Laser synthesis and processing of colloids: fundamentals and applications, Chem. Rev. 117 (2017) 3990–4103.
 [45] (a) H. Zeng, X. Du, S.C. Singh, S.A. Kulinich, S. Yang, J. He, W. Cai, Nano-
- [45] (a) H. Zeng, X. Du, S.C. Singh, S.A. Kulinich, S. Yang, J. He, W. Cai, Nano-materials via laser ablation/irradiation in liquid: a review, Adv. Funct. Mater. 22 (2012) 1333–1353;
 - (b) S.C. Singh, H. Zeng, Nanomaterials and nanopatterns based on laser processing: a brief review on current state of art, Sci. Adv. Mater. 4 (2012) 368–390.
- [46] S. Barcikowski, G. Compagnin, Advanced nanoparticle generation and excitation by lasers in liquids, Phys. Chem. Chem. Phys. 15 (2013) 3022–3026.
- [47] (a) S.C. Singh, H. Zeng, S. Yang, et al., Nanomaterials: laser—based processing in liquid media, in: S.C. Singh, H. Zeng, C. Guo, et al. (Eds.), Nanomaterials: Processing and Characterization with Lasers, Wiley-VCH Verlag & Co. KGaA, Weinheim, Germany, 2012, pp. 317—494;
 - (b) M. Dell'Aglio, A. De Giacomo, Plasma charging effect on the nanoparticles releasing from the cavitation bubble to the solution during nanosecond Pulsed Laser Ablation in Liquid, Appl. Surf. Sci. 515 (2020) 14603.
- [48] G.W. Yang, Laser ablation in liquids: applications in the synthesis of nanocrystals, Prog. Mater. Sci. 52 (2007) 648–698.
- [49] H. Muto, K. Yamada, K. Miyajima, F. Mafuné, Estimation of surface oxide on surfactant-free gold nanoparticles laser-ablated in water, J. Phys. Chem. C 111 (2007) 17221–17226.
- [50] J.P. Sylvestre, S. Poulin, A.V. Kabashin, E. Sacher, M. Meunier, J.T.H. Luong, Surface chemistry of gold nanoparticles produced by laser ablation in aqueous media, J. Phys. Chem. B 108 (2004) 16864.
- [51] Z. Li, Y. Zhang, Y. Feng, C. Cheng, K. Qiu, C. Dong, H. Liu, X. Du, Co3O4 nanoparticles with ultrasmall size and abundant oxygen vacancies for boosting oxygen involved reactions, Adv. Fun. Mater. 29 (2019) 1903444.
- [52] J. Johny, S.S. Guzman, B. Krishnan, J.A.A. Martinez, D.A. Avellaneda, S. Shaji, SnS2 nanoparticles by liquid phase laser ablation: effects of laser fluence, temperature and post irradiation on morphology and hydrogen evolution reaction, Appl. Surf. Sci. 470 (2019) 276–288.
- [53] A. Neumeister, J. Jakobi, C. Rehbock, J. Moysig, S. Barcikowski, Monophasic ligand-free alloy nanoparticles synthesis determinants during pulsed laser ablation of bulk alloy and consolidated microparticles in water, Phys. Chem. Chem. Phys. 16 (2014) 23671.
- [54] M.S.S. Bharati, C. Byram, V.R. Soma, Femtosecond laser fabricated Ag@Au and Cu@Au alloy nanoparticles for surface enhanced Raman spectroscopy based trace explosives detection, Front. Phys. 6 (2018) 28.
- [55] J. Lian, Y. Wu, H. Zhang, S. Gu, Z. Zeng, X. Ye, One-step synthesis of amorphous Ni-Fe-P alloy as bifunctional electrocatalyst for overall water splitting in alkaline medium, Int. J. Hydrogen Energy 43 (2018) 12929–12938.

- [56] (a) A. Shukla, A.K. Bhardwaj, B.K. Pandey, S.C. Singh, K.N. Uttam, J. Shah, R.K. Kotnala, R. Gopal, Laser synthesized magnetically recyclable titanium ferrite nanoparticles for photodegradation of dyes, J. Mater. Sci. Mater. Electron. 28 (20) (2017) 15380–15386;
 - (b) R.K. Swarnkar, S.C. Singh, R. Gopal, Optical characterizations of copper oxide nanomaterial, International Conference on Optics and Photonics, Chandigarh, India, 2009.
- [57] (a) A. Shukla, B.K. Pandey, S.C. Singh, K.N. Uttam, J. Shah, R.K. Kotnala, A. Kumar, R. Gopal, Liquid-assisted pulsed laser ablation synthesis of titanium ferrite nanomaterials, Mater. Focus 4 (2015) 327–332;
 (b) R.K. Swarnkar, S.C. Singh, R. Gopal, Synthesis of copper/copper-oxide
- (b) R.K. Swarnkar, S.C. Singh, R. Gopal, Synthesis of copper/copper-oxide nanoparticles: optical and structural characterizations, AIP Conf. Pro 1147 (2009) 205–210.
 [58] (a) S.C. Singh, R.K. Kotnala, R. Gopal, Room temperature ferromagnetism in
- liquid-phase pulsed laser ablation synthesized nanoparticles of nonmagnetic oxides, J. Appl. Phys. 118 (2015), 064305; (b) S.C. Singh, Effect of oxygen injection on the size and compositional evolution of ZnO/Zn (OH) 2 nanocomposite synthesized by pulsed laser ablation in distilled water, J. Nanopart. Res. 13 (2011) 4143–4152. [59] (a) A. Shukla, S.C. Singh, B.K. Pandey, K.N. Uttam, J. Shah, R.K. Kotnala, R. Gopal,
- [39] (a) A. Shuka, S.C. Singh, B.K. Pandey, K.N. Ottam, J. Shah, K.K. Kothala, K. Gopal, Liquid-assisted pulsed laser ablation synthesized titanium ferrite nanoparticles: structural, optical and magnetic properties, Adv. Mater. Lett. 6 (2015) 1066–1072;
 (b) R.K. Swarnkar, S.C. Singh, R. Gopal, Optical characterizations of copper
 - (b) K.K. Swarnkar, S.C. Singh, R. Gopal, Optical characterizations of copper oxide nanomaterial, International Conference on Optics and Photonics, Chandigarh, India, 30, 2009.
- [60] D.M. Arboleda, J.M.J. Santillán, L.J.M. Herrera, M.B.F. Raap, P.M. Zélis, D. Muraca, D.C. Schinca, L.B. Scaffardi, Synthesis of Ni nanoparticles by femtosecond laser ablation in liquids: structure and sizing, J. Phys. Chem. C 23 (2015) 13184–13193.
- [61] http://database.iem.ac.ru/mincryst/.
- [62] E. Lohrasbi, M. Asgari, Electrooxidation of urea on the nickel oxide nanoparticles and multi-walled carbon nanotubes modified screen printed electrode, Adv. Anal. Chem. 5 (3A) (2015) 9–18.
- [63] J.C. Bear, P.D. McNaughter, P. Southern, P. O'Brien, C.W. Dunnill, Nickel-doped ceria nanoparticles: the effect of annealing on room temperature ferromagnetism, Crystals 5 (2015) 312–326.
- [64] https://www.crystallography.net/cod/search.html.
- [65] M. Thirumoorthia, J.T. Joseph Prakash, Structure, optical and electrical properties of indium tin oxide ultra thin films prepared by jet nebulizer spray pyrolysis technique, J. Asian Ceram. Soc. 4 (2016) 124–132.
- [66] S.C. Singh, R. Gopal, Nanoarchitectural evolution from laser-produced colloidal solution: growth of various complex cadmium hydroxide architectures from simple particles, J. Phys. Chem. C 114 (2010) 9277–9289.
- [67] S.C. Singh, R. Gopal, Drop shaped zinc oxide quantum dots and their selfassembly into dendritic nanostructures: liquid assisted pulsed laser ablation and characterizations, Appl. Surf. Sci. 258 (2012) 2211–2218.
- [68] A. Shukla, A.K. Bhardwaj, S.C. Singh, K.N. Uttam, N. Gautam, A.K. Himanshu, J. Shah, R.K. Kotnala, R. Gopal, Microwave assisted scalable synthesis of titanium ferrite nanomaterials, J. Appl. Phys. 123 (2018) 161411.
- [69] M. Ramesh, M.P.C. Rao, S. Anandan, H. Nagaraj, Adsorption and photocatalytic properties of NiO nanoparticles synthesized via a thermal decomposition process, J. Mater. Res. 33 (2018) 601–610.
- [70] H.B. Li, M.H. Yu, F.X. Wang, P. Liu, Y. Liang, J. Xiao, C.X. Wang, Y.X. Tong, G.W. Yang, Amorphous nickel hydroxide nanospheres with ultrahigh capacitance and energy density as electrochemical pseudocapacitor materials, Nat. Commun. 4 (2013) 1894.
- [71] V. Vedharathinam, G.G. Botte, Direct evidence of the mechanism for the electro-oxidation of urea on Ni(OH)2 catalyst in alkaline medium, Electrochim. Acta 108 (2013) 660–665.
- [72] S. Deabate, F. Fourgeot, F. Henn, X-ray diffraction and micro-Raman spectroscopy analysis of new nickel hydroxide obtained by electrodialysis, J. Power Sources 87 (2000) 125–136.
- [73] D.S. Hall, D.J. Lockwood, C. Bock, B.R. MacDougall, Nickel hydroxides and related materials: a review of their structures, synthesis and properties, Proc. R. Soc. A. 471 (2015) 20140792.
- [74] W. Guo, B. Liu, Liquid-phase pulsed laser ablation and electrophoretic deposition for chalcopyrite thin-film solar cell application, ACS Appl. Mater. Interfaces 4 (2012) 7036–7042.
- [75] Tadashi Uchida, Yukio Kurita, Naokazu Koizumi, Masaji Kubo, J. Polym. Sci. XI (1956) 313–322.
- [76] G. Ou, P. Fan, H. Zhang, K. Huang, C. Yang, W. Yu, H. Wei, M. Zhong, H. Wu, Y. Li, Large-scale hierarchical oxide nanostructures for high-performance electrocatalytic water splitting, Nano Energy 35 (2017) 207–214.
- [77] K. Fominykh, J.M. Feckl, J. Sicklinger, M. Döblinger, S. Böcklein, J. Ziegler, L. Peter, J. Rathousky, E. Scheidt, T. Bein, D.F. ng, Ultrasmall dispersible crystalline nickel oxide nanoparticles as high-performance catalysts for electrochemical water splitting, Adv. Funct. Mater. 24 (2014) 3123–3129.
- [78] R. Zhang, H. Wei, W. Si, G. Ou, C. Zhao, M. Song, C. Zhang, H. Wu, Enhanced electrocatalytic activity for water splitting on NiO/Ni/carbon fiber paper, Materials 10 (2017) 15.
- [79] Aniruddha Mondal, Anirban Paul, Divesh N. Srivastava, Asit B. Panda, NiO hollow microspheres as efficient bifunctional electrocatalysts for Overall Water-Splitting, Int. J. Hydrogen Energy 4 3 (2018) 2 1 6 6 5–2 1 6 7 4.

- [80] Xiaodong Yan, Lihong Tian, Xiaobo Chen, Crystalline/amorphous Ni/NiO core/shell nanosheets as highly active electrocatalysts for hydrogen evolution reaction, J. Power Sources 300 (2015) 336–343.
- [81] J. Wang, S. Mao, Z. Liu, Z. Wei, Haiyan Wang, Yiqing Chen, Yong Wang, Dominating role of NiO on the interface of Ni/NiO for enhanced hydrogen evolution reaction, ACS Appl. Mater. Interfaces 9 (2017) 7139–7147.
- [82] Ming Gong, Zhou Wu, Mon-Che Tsai, Jigang Zhou, Mingyun Guan, Meng-Chang Lin, Bo Zhang, Yongfeng Hu, Di-Yan Wang, Yang Jiang, Stephen J. Pennycook, Bing-Joe Hwan, Hongjie Dai, Nanoscale Nickel oxide/nickel heterostructures for active hydrogen evolution electrocatalysis, Nat. Commun. 5 (2014) 4695, https://doi.org/10.1038/ncomms5695.
- [83] W. Sheng, M. Myint, J.G. Chen, Y. Yan, Correlating the hydrogen evolution reaction activity in alkaline electrolytes with the hydrogen binding energy on monometallic surfaces, Energy Environ. Sci. 6 (2013) 1509–1512.
- [86] A. Singh, N.B. Singh, I. Hussain, H. Singh, V. Yadav, S.C. Singh, Green synthesis of nano zinc oxide and evaluation of its impact on germination and metabolic activity of Solanum lycopersicum, J. Biotechnol. 233 (2016) 84–94, https://doi.org/10.1016/j.jbiotec.2016.07.010.
- [87] S.C. Singh, et al., Structural and compositional control in copper selenide nanocrystals for light-induced self-repairable electrodes, Nano Energy 51 (2018) 774–785.
- [88] N.B. Singh, et al., Zinc oxide nanoparticles as fertilizer for the germination, growth and metabolism of vegetable crops, J. Nanoeng. Nanomanufact. 3 (2013) 353–364.
- [89] D. Singh, et al., Applications of liquid assisted pulsed laser ablation synthesized TiO2 nanoparticles on germination, growth and biochemical parameters of Brassica Oleracea var. Capitata, Sci. Adv. Mater. 4 (2012) 522–531.
- [90] N. Amist, et al., Comparative studies of Al3+ ions and Al203 nanoparticles on growth and metabolism of cabbage seedlings, J. Biotechnol. 254 (2017) 1–8.